Unlocking the electrochemical performance of glassy carbon electrodes by surface engineered, sustainable chitosan membranes

Agata Smułka [a], Mateusz Cieślik [a,d], Adrian Olejnik [b], Artur Zieliński [c], Jacek Ryl [d,*], Tadeusz Ossowski [a]

[a] *Department of Analytical Chemistry, University of Gdańsk, Wita Stwosza 63, 80-308 Gdańsk, Poland*
[b] *Department of Metrology and Optoelectronics, Gdańsk University of Technology, Narutowicza 11/12, 80-233 Gdańsk, Poland*
[c] *Department of Electrochemistry, Corrosion and Materials Engineering, Gdańsk University of Technology, 80-233 Gdańsk, Poland*
[d] *Division of Electrochemistry and Surface Physical Chemistry, Faculty of Applied Physics and Mathematics, Gdańsk University of Technology, Narutowicza 11/12, Gdańsk 80-233, Poland*

ARTICLE INFO

ABSTRACT

Chitosan coatings, derived from crustacean shell waste, possess inherent biocompatibility and biodegradability, rendering them suitable for various biomedical and environmental applications, including electrochemical biosensing. Its amine and hydroxyl functional groups offer abundant sites for chemical modifications to boost the charge transfer kinetics and provide excellent adhesion, enabling the construction of robust electrode-coating interfaces for electroanalysis. This study explores the role of electrostatically-driven chemical interactions and crosslinking density originating from different chitosan (Cs) and glutaraldehyde (Ga) concentrations in this aspect. Studying anionic ($[Fe(CN)_6]^{3-/4-}$), neutral ($FcDM^{0/+}$), and cationic ($[Ru(NH_3)_6]^{2+/3+}$) redox probes highlights the influence of Coulombic interactions with chitosan chains containing positively-charged pathways, calculated by DFT analysis. Our study reveals how a proper Ch-to-Ga ratio has a superior influence on the crosslinking efficacy and resultant charge transfer kinetics, which is primarily boosted by up to 20× analyte preconcentration increase, due to electrostatically-driven migration of negatively charged ferrocyanide ions toward positively charged chitosan hydrogel. Notably the surface engineering approach allows for a two-orders of magnitude enhancement in $[Fe(CN)_6]^{4-}$ limit of detection, from 0.1 μM for bare GCE down to even 0.2 nM upon an adequate hydrogel modification.

1. Introduction

Among recent literature reports, there has been rapid growth in the interest in electroanalysis techniques, due to their high sensitivity and efficiency in the determination of trace analytes. Electrochemical techniques allow for molecular recognition of different analytes, providing detailed information on their nature. At the same time, there is a growing demand for sensing devices, primarily featuring fast, low-cost, and automatic stand-alone solutions [1]. Electrochemical sensors, which offer portability and allow for miniaturization to reduce sample and solvent volumes have significant potential to fill this gap [2]. The search for sensors with the best possible reproducibility, sensitivity, detection limit, or quantification is stimulating the electrode materials engineering and development [3]. Conventional carbon electrodes such as glassy carbon [4], carbon paste [5], graphene [6], and diamond [7], enabled

the intensive development of electrochemical sensors, but have not overcome the growing challenges of finding more selective and sensitive methods. Along with the solution comes the modification of electrodes affecting the expansion of the active surface, the reduction of charge transfer resistance or the kinetics of electrode processes to improve sensitivity or detection selectivity.

Nanomaterials have higher adsorption capacity due to the preferable surface-to-volume ratio, often offering electrocatalytic activity [8]. Formation of heterojunctions by decorating nanomaterials on the electrode surface or introducing it to composite structures offers promising opportunities for electrode modification that can contribute to the creation of new electrochemical sensors [9–11]. A popular way to modify the surface of electrodes is to fabricate or apply membranes or films to the surface [12,13]. It is possible to fabricate composite membranes on the surface of an electrode for use in biological sensors containing

proteins. Composites containing nanocellulose and carbon nanotubes have been used, contributing to the monitoring of small particles in biological environments [14].

One of the most promising surface engineering techniques is the modification of electrode surfaces with hydrogels. Hydrogels are attractive materials in sensory terms; they are water-rich, hydrophilic polymer networks, and their properties can be easily modified. In addition, some of them undergo conformational changes under the influence of external stimuli, such as temperature, pH, or the presence of certain substances [15]. They are applied to electrode surfaces in the form of thin films in which specific compounds can be placed to improve detection and sensor sensitivity [16]. Such systems were recognized to be effective in advanced drug delivery systems, electrochemical actuators [17], or bioelectronic device design [18]. For example, aptamer introduced into a poly(acrylic acid) hydrogel enabled the effective detection of diclofenac [19]. Stable hydrogel layers may be used for the physical entrapment of enzymes in catalytically driven biosensors, offering receptor grafting while at the same time reducing the electrode fouling. Such a strategy was used to develop electrochemical biosensors for the detection of ethanol, glucose, NADH, and more [20].

Chitosan is a natural biopolymer that has recently come under the spotlight for a range of properties, including antimicrobial [21], antiviral [22], antifungal [23], mucoadhesive [24], biodegradable [25] and biocompatible [26]. It is obtained as a by-product, mainly in the food industry, making it cheap and fitting for green chemistry. Various properties can affect the characteristics of the resulting chitosan hydrogel, so attention should be paid to its purity, crystallinity, water content, and especially the degree of deacylation and molecular weight [27]. Containing amino and hydroxyl groups, chitosan chains can be easily modified via covalent or physical bonding. Chitosan's popularity is related to its ability to form hydrogels [28], films [29], and nanoparticles [30] while maintaining ionic conductivity [31]. The use of chitosan for the production of coatings/films/scaffolds, in which it acts mainly as a carrier, in electrochemistry is an important issue [32]. Hydrogel structures have been successfully used in sensors due to the possibility of including specific centers inside and on the surface [33,34]. Cross-linked chitosan hydrogels dissolved in organic acids are considered to be stable [35,36]. Moreover, chitosan polymer network may be decorated with nanoparticles [37], organic or inorganic cross-linking fragments, and coordination centers of large biomolecular systems, driven by electrostatic interactions and opening the route to fabricate structures capable of selective interactions with a wide range of analytes [38].

This work aims to discuss how cheap and rapid surface engineering by chitosan hydrogel coating affects the charge transfer mechanism. We provide an in-depth description of how chitosan and glutaraldehyde content influence the cross-linking density, identifying how electrostatic-driven interactions between hydrogel coating and different redox probes affect the charge transfer kinetics at the electrode/electrolyte interface and resultant utility of proposed surface engineering.

2. Experimental

2.1. Materials and reagents

All chemicals were of analytical grade and used as received without further purification. Chitosan low molecular weight (Ch), acetic acid (AA), glutaraldehyde (Ga), potassium chloride (KCl), potassium hexacyanoferrate(III) $K_3[Fe(CN)_6]$, potassium hexacyanoferrate(II) $K_4[Fe(CN)_6]$, 1,1′-ferrocenedimethanol $C_{12}H_{14}FeO_2$ and hexaamineruthenium chloride $[Ru(NH_3)_6]Cl_2$ were received from Sigma Aldrich. Phosphate-buffered saline (PBS) with concentration 0.01 M and a pH = 7 from ThermoFisher Scientific was obtained by dissolving tablets in deionized water.

2.2. Preparation of chitosan hydrogel

A mass of chitosan was suspended in the AA 1 % solution. The mixture was left on a magnetic stirrer, for 24 h, until the chitosan dissolved. Then Ga (1 % solution) was added into Cs solution. Thus, a series of hydrogels were prepared with the compositions given in Table 1.

2.3. Physico-chemical measurements and simulations

Fourier-transform infrared (FT-IR) spectroscopy analysis was carried out with a Bruker IFS66 spectrometer. The spectra were obtained in the spectral range 5000–400 cm^{-1}. Samples were prepared by the standard CaF$_2$ pellet method. X-ray Photoelectron Spectroscopy (XPS) analysis was carried out with Escalab 250Xi (ThermoFisher Scientific), operating AlKα source and 250 μm spot diameter, under low-energy e$^-$ and Ar$^+$ flow for charge compensation. Peak deconvolution was done in Avantage v.59921 provided by the spectroscope manufacturer, with final calibration on adventitious carbon *C 1s* at 284.7 eV.

The contact angle was measured using a Kruss (Hamburg, Germany) DSA100 goniometer. Samples for measurements were prepared by applying 5 μL of hydrogel to a glass plate and allowed to evaporate at room temperature. A 4 μL drop of water was applied to the surface thus created using a syringe. The contact angle on both sides of the droplet was then measured using a CCD camera, and the average contact angle was determined with ADVANCE software using the Young-Laplace method. Each measurement was repeated 20 times. Kinematic viscosity was measured using a 4-mm diameter flow cup. 100 ml each of hydrogel and acetic acid solutions were prepared. Each liquid at room temperature was passed through the effluent cup, the flow time was measured using a stopwatch. Each measurement was repeated 3 times.

Kinematic viscosity was determined according to the ASTM standard [39]. The ζ-potential was measured using the Electrophoretic Light Scattering method (ELS). Measurements were carried out on the Litesizer 500, ANTON-PAAR for ELS > ±1000 mV. Transmission electron microscopy (TEM) images were performed using a Tecnai G2 Spirit BioTWIN by FEI operated at 120 kV.

Atomic Force Microscopy (AFM) imaging was performed using NTegra Prima (NT-MDT, Russia). To enable scanning a surface of GCEs, a dedicated holder was made, adapted to be mounted in the base of the atomic force microscope and performing measurements in scan-by-head configuration. To minimize the probe interaction with the hydrogel surface, a semi-contact mode ("tapping") of scanning was utilized, by oscillating the AFM probe near its resonance frequency. This intermittent contact reduces the lateral forces between the probe and the sample, minimizing potential damage to the surface. The amplitude of the cantilever oscillation is monitored during scanning using a feedback loop. Probes NSG30 (TipsNano) were used. Their geometric parameters

Table 1

Representation of samples with different Cs-to-Ga ratios in the studied hydrogel coatings. Columns represent constant chitosan concentrations, and rows represent the proportion of glutaraldehyde in the hydrogel. The first row corresponds to hydrogels containing no crosslinker.

	Content % (w/w) chitosan			
	0.37	0.53	0.78	1
Content % (w/w) glutaraldehyde	–	–	–	–
	C1A0	C2A0	C3A0	C4A0
	0.75	1.04	1.48	1.96
	C1A1	C2A1	C3A1	C4A1
	1.34	2.01	3.01	3.92
	C1A2	C2A2	C3A2	C4A2
	2.03	3.00	4.30	5.66
	C1A3	C2A3	C3A3	C4A3
	3.42	5.67	8.14	10.53
	C1A4	C2A4	C3A4	C4A4
	3.83	8.32	11.65	15.02
	C1A5	C2A5	C3A5	C4A5

are as follows: cantilever length 125 ± 10 mm, width 30 ± 7.5 mm, thickness 4 ± 7.5 mm, tip curvature radius 10 nm. The resonant frequency is 244.5 kHz. Each measurement was represented by two maps: a topographic and a deflection (DFL), showing changes in the oscillation amplitude. Since the tubular shape of the piezoelectric scanner creates an artificial skew in the obtained images, they were processed by removing the second-degree polynomial curve for each horizontal scan line. After performing this procedure, the algebraic (Ra) roughness was calculated for the corrected images following the ISO 4287/1 standard. Ra is the arithmetic mean of deviations from the average surface profile $|\delta(x)|$ in accordance with the quantity defined using the relationship described by the Eq. (1):

$$R_a = \frac{1}{L} \int_0^L |\delta(x)| \, dx \tag{1}$$

In the discrete form used for calculations, the parameter L = 5 μm corresponds to the length of the image edge, while dx is approximated with a surface sampling step of 19.65 nm. As in traditional surface metrology, the parameter used is one of the ways to express the degree of surface development. The average pore size (Rp) was determined using Gwyddion 2.63 software (https://gwyddion.net/). Structures with a height lower than 40 % of the average level in the image were assumed as pores, based on the thresholding of the topographic image.

Molecular configurations of chitosan were constructed using the Atomistic ToolKit Quantumwise (ATK, Synopsys, USA). Specifically, chitosan chains composed of 9 structural units were employed as the primary model. DFT-optimized geometries and corresponding electrostatic surface potential (ESP) maps were calculated for both neutral and amine-protonated single molecules in pyranose configurations.

Additionally, a fully periodic cell containing 4 chitosan chains (36 structural units) was built and filled with water molecules to model the electrostatic environment inside the hydrogel (1517 atoms in total). The water packing was accomplished utilizing the Packmol plugin, ensuring perfect packing with a 2 Å buffer layer, with the number of molecules adjusted accordingly [40]. The cell was optimized using a DREIDING forcefield and the ESP map was calculated by density functional theory (DFT). DFT calculations were conducted via ATK software utilizing the Perdew–Burke–Ernzerhof (PBE) exchange–correlation functional, operating within the generalized gradient approximation framework as incorporated within the computational package. Pseudo-Dojo pseudopotentials were applied with double-zeta polarized basis functions, 125 Ha density-mesh cutoff, and $4 \times 4 \times 4$ k-point mesh.

2.4. Electrochemical studies

The glassy carbon electrode (GCE, 3.0 mm diameter) was first polished with Al_2O_3 powder (0.3 mm) using a polishing kit from Buehler, rinsed with deionized water from Hydrolab Poland, and then dried under a continuous stream of nitrogen at room temperature. Then 5 μL of chitosan hydrogel was applied to the surface thus prepared using an automatic pipette and dried in a stream of nitrogen at room temperature for 30 min. The measuring system consisted of a self-designed vessel, the GCE and Ag/AgCl electrodes from Mineral, and the Pt wire came from Mennica Polska.

These measurements were taken using a Methron Autolab potentiostat/galvanostat, M204 equipped with FRA32M electrochemical impedance spectroscopy module with operating system Nova 2.15. The electrochemical studies of the prepared electrodes were evaluated in a three-electrode system, with a modified GCE as a working electrode, an Ag/AgCl (0.1 M KCl) reference electrode, and a platinum mesh as a counter electrode. The influence of surface engineering by hydrogel coating on the electrode kinetics was evaluated using cyclic voltammetry (CV), differential pulse voltammetry (DPV), and electrochemical impedance spectroscopy (EIS). Electrochemical studies were carried out with 1 mM $K_3[Fe(CN)_6]$, $[K_4Fe(CN)_6]$, $C_{12}H_{14}FeO_2$, and $[Ru(NH_3)_6]Cl_2$

dissolved in 0.1 M KCl or PBS as the primary electrolyte. Cyclic voltammograms were registered with scan rates between 10 and 1000 mV/s, and in the potential range -0.35 V to 0.65 V. DPV experimental conditions were: scan rate 10 mV/s, step potential 0.005 V, modulation amplitude 0.025 V, modulation time 0.05 s and interval time 0.5 s, polarization range from -0.3 V to 0.8 V.

3. Results and discussion

3.1. Hydrogel cross-linking effect on its physicochemical characteristics

The crosslinking density of a hydrogel structure affects its physical and rheological properties, transport of ions, and electrostatic charge distribution within the coating, affecting the material's viscosity, density, and hydrophilicity. The hydrogel layer can be treated as a hydromembrane, where the surface properties and the structure of the layer itself determine the migration through the coating, electrostatic interactions, or the system of internal and external hydrogen bonds.

FTIR studies were performed to confirm the derivation of chitosan hydrogels. Fig. 1 shows FT-IR spectra for hydrogels at different Ga (Fig. 1a) and Cs (Fig. 1d) content. Spectrum labeled as "C" is attributed to dry chitosan powder. Within all studied samples, the broadband region located about 3400 cm^{-1} results from the stretching vibration of the hydroxyl group (–OH) and stretching N–H vibration. The double band located at 2935–2864 cm^{-1} results from the C–H stretching vibration. The band located 1709 and 1656 cm^{-1} results from the normal stretching C=O. The band located around 1550 cm^{-1} results from an amide band, appearing as a result of interactions between N–H bending vibrations and C–N stretching vibrations. The band located around 1410–1389 cm^{-1} results from the aldehyde bending vibration C–H, this signal is invisible in the case of dry chitosan. In cross-linked chitosan hydrogels, it is much more pronounced. The medium intensity band located at 1155 cm^{-1} results in an uncoupled C–N bond in amines, formed by coupling the stretching vibration of the C–N with the stretching vibration of an adjacent bond in the molecule. The band located around 1050–1019 cm^{-1} results in C–O–C vibrations in the glycosyl units [41,42]. In summary, absorbance peaks for the OH$^-$ group are clearly more intense when compared to powdered chitosan, suggesting hydrogel formation, which is the total of both the signal from the sugar chitosan units and the water-forming hydrogel. The appearance of absorbance peaks at wavelengths corresponding to glutaraldehyde, confirms the presence of cross-linked hydrogel structures.

The high-resolution XPS spectra recorded for the C2A2 sample in the *C 1s* and N 1s region reveal the surface chemical composition of the hydrogel coating. The primary *C 1s* component at 284.7 eV is characteristic of C–C aliphatic bonds in Cs and Ga, while its share is usually inflated by adventitious carbon due to exposure to air [43,44]. The remaining *C 1s* spectral components show the share of oxidized C-OH, C-OC, CN=C, and C=OC moieties [45], contributing 43.7 at.% and indicating the hydrogel presence, yet with stoichiometry weakly corresponding to the used Cs and Ga content. On the other hand, N 1 spectra (in Fig. 1**c** inset) reveal the presence of primary amines (BE at 399.7 eV) [46] and protonated alkyl ammonium R–NH$_3^+$ species (BE at 402.1 eV) [47] with 1.7:1 ratio of total [N]. The total share of [N] species was equal to approx. 3.7 at.%.

The presence of –NH$_3^+$ moieties in the chitosan chain was confirmed with XPS. The accelerated migration of the redox probe in the vicinity of –NH$_3^+$ moieties is expected due to Coulombic attraction. On the other hand, the positively charged moieties are expected to associate with negatively charged $[Fe(CN)_6]^{3-/4-}$. Overall, however, we observe the ease of transport of negatively charged redox probe through the positively charged hydrogel structure [48]. The diffusion coefficient D is related to viscosity η of the system through the radius r of the moving particle as defined by the Stokes-Einstein Eq. (2):
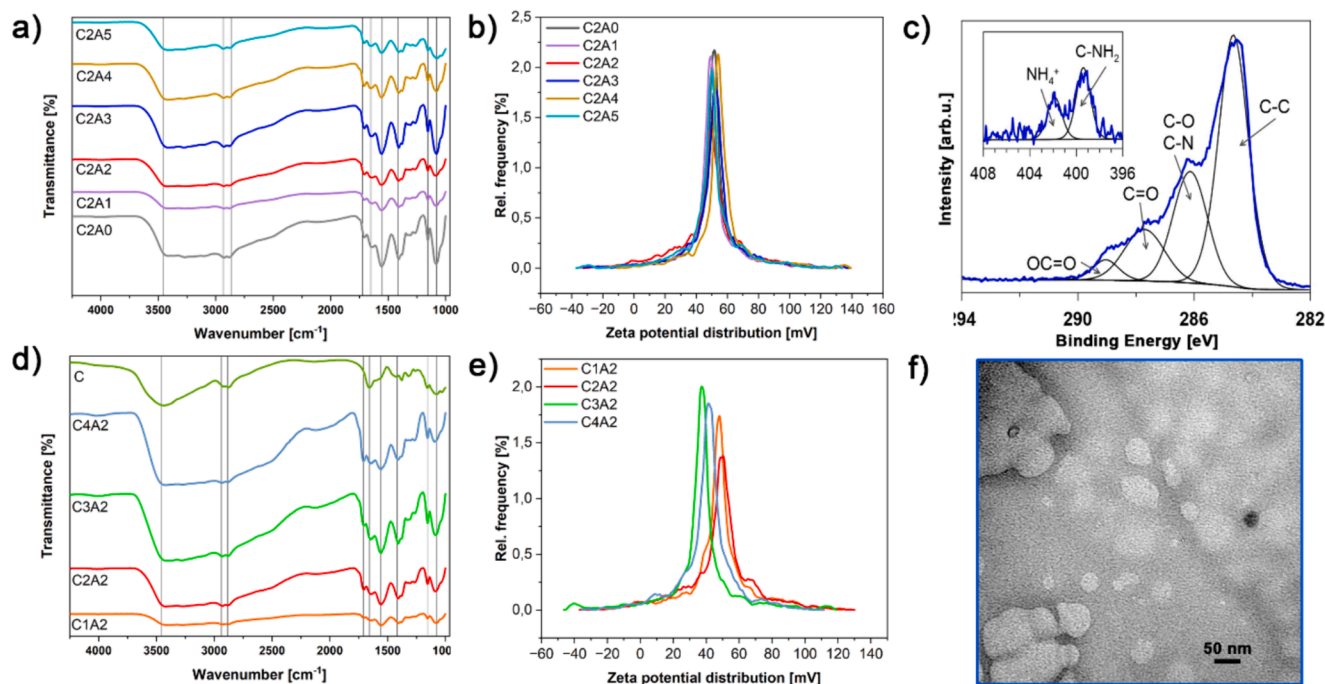
$$D = \mathscr{k}T/6\pi\eta r \tag{2}$$

Fig. 1. a,d) FTIR spectra and b,e) ζ-potential analyses carried out for chitosan hydrogel coatings surface engineered with varying content of a,b) Ad crosslinker, d,e) Cs chains; c) high-resolution XPS *C 1s* and *N 1s* spectra and f) HR-TEM micrograph of C2A2 hydrogel coating.

where r is the radius of the diffusing species, $\mathcal{k}$ is the Boltzmann constant, and T is temperature.

The measurements performed using a flow cup were aimed at determining the influence of Cs chains and Ad cross-linker content on the viscosity changes of the prepared hydrogels. The obtained results were calculated according to ASTM standard [39] and are presented in Table 2. The above-described studies clearly show that cross-linker content has negligible influence on as-measured hydrogel viscosity η. On the other hand, hydrogel viscosity increases approximately linearly with the increase of chitosan concentration, marking it as a potentially primary parameter affecting the D value.

Measuring ζ-potential is very informative when analyzing the stability of colloidal systems. A suspended colloidal (or hydrogel) system is considered stable if the ζ-potential value is greater than +25 mV or less than −25 mV. For values between +25 and −25 mV, the system is considered unstable. Each of the studied chitosan hydrogels is characterized by ζ-potential values above 25 mV. The ζ-potential values of the hydrogels oscillate between 34.76 mV (C3A2), and 49.42 mV (C2A3), as shown in Fig. 1b and e. The measured ζ-potential values and the differences between them may be due to the different pH values of the individual chitosan hydrogels, and mainly to the different amounts of protonated and deprotonated amino and hydroxyl groups. The presence of positively charged amine groups can cause the measured ζ-potentials to take on positive values. As the chitosan content of the hydrogel

increases (from C1 to C4), the number of secondary amino groups increases. It can be expected that under neutral pH conditions, they are predominantly protonated. Consequently, the charge accumulated in the hydrogel layer increases, increasing the strength of electrostatic interactions in the gel. The consequence is an increase in disorder in the structure of the hydrogel and a slight change in its stability. Changes in the value of ζ-potentials are also compounded by the presence of charges at the boundaries of the mers (the basic building unit of the chitosan polymer, β-(1,4)-D-glucosamine) (Fig. 1e) affecting charge, and mass migration.

To determine the hydrophilicity of chitosan hydrogel coatings, a series of contact angle (CA) measurements were carried out. The wettability of any surface can vary based on its chemical nature and topography. The obtained average values of the contact angles of the analyzed hydrogel surfaces differ significantly depending on cross-linking density, and are in the range from 56.43° to 94.20°, see Table 2. Expectedly, different Cs concentrations present in AA had no obvious effect on hydrogel hydrophilicity due to negligible changes in chemistry, with CA indicating the hydrophilic behavior of each formed coating except for C2A0. Here, the role of Ga as the cross-linking agent seems to be dominant. Its presence appears to be necessary to obtain hydrophilic properties and is mainly related to the formation of more densely cross-linked conjugates with higher Ga content. Interestingly, the Ga content within the hydrogel plays a pivotal role at low

Table 2
Physico-chemical (ζ, CA), rheology (η), and topography (Ra) changes, illustrating the influence of Cs chains and Ga cross-linker content.

| | GCE | varying Ga content | | | | | | varying Cs content | | | |
		C2A0	C2A1	C2A2	C2A3	C2A4	C2A5	C1A2	C2A2	C3A2	C4A2
η/mm²s⁻¹	–	3.38 ± 0.14	3.28 ± 0.49	3.15 ± 0.10	3.35 ± 0.13	3.49 ± 0.21	3.48 ± 0.40	2.65 ± 0.22	3.15 ± 0.10	4.43 ± 0.20	6.31 ± 0.19
ζ/mV	–	49.01 ± 2.2	47.03 ± 1.8	47.07 ± 1.7	49.42 ± 1.3	48.77 ± 1.7	46.92 ± 1.9	45.87 ± 1.6	47.07 ± 1.7	34.76 ± 4.6	41.97 ± 3.0
CA/°	72.00 ± 0.54	94.20 ± 0.88	81.47 ± 2.70	56.43 ± 2.05	71.10 ± 1.86	65.38 ± 1.42	65.19 ± 1.30	80.13 ± 2.29	56.43 ± 2.05	74.70 ± 0.51	75.22 ± 2.23
Ra/nm	5.4	2.4	0.7	1.3	0.5	0.6	1.7	11.4	1.3	1.7	1.5
Rp/nm	–	198	n/a	n/a	68	78	608	438	n/a	96	n/a

concentrations, when it saturates at approx. 56–65° between samples C2A2 and C2A5. A similar behavior was observed for other Cs-based hydrogels [49,50]. The contact angle value is inversely proportional to the permeation rate, constituting an important factor when considering the mass transport through the hydrogel membrane and the electro-chemically active surface area of the electrode [51].

The image obtained with a transmission electron microscope shows the structure of the C2A2 hydrogel. The addition of glutaraldehyde to the hydrogel is intended to organize the close-range polymeric networks of the structure. Ordered structures are expected, and this has been verified at the nanoscale; it turns out that slight differences in structure are produced, as the image shows areas where the hydrogel forms local agglomerates as shown in Fig. 1f.

Due to the presence of networks in hydrogels and the ability to diffuse water molecules, all swollen hydrogels are considered porous materials. Porosity is influenced by the type of polymer, its amount, and the presence of a cross-linking agent. Macroporous hydrogels have the highest amount of unbound water at the expense of the solid parts of the hydrogel, resulting in weaker mechanical properties [52]. The presence of pores in the materials promotes the formation of an electric double layer, due to the increased availability of adsorbing sites for ions, facilitating their transport. Macroporous materials can behave as buffer reservoirs for electrolyte ions, affecting the distances of ions to the surface of the electrode material, and resulting in changes in their diffusion [53,54]. The porous structure of the hydrogel creates transport channels providing better access to the electrode surface, while on the other hand introducing microscopic sites of surface electric heteroge-neities, possibly leading to deteriorated and complex electrode kinetics [55,56]. Explicit evidence of the presence of pores in the analyzed hydrogels was obtained from AFM images, presented in Fig. 2.

The AFM maps reveal the fundamental importance of the proper Cs-to-Ga ratio to achieve effecting hydrogel cross-linking. Too large of a glutaraldehyde content consequences in coating heterogeneity, man-ifested by the appearance of micro-scaled pores as seen in particular for

C1A2 (Fig. 2a) and C2A5 (Fig. 2f) samples. The higher the Cs-to-Ga ratio the more homogeneous the hydrogel coating, with much smaller vari-ation in its surface roughness and absence of micro-sized pores. The average pore size Rp and surface roughness Ra are depicted in Table 2.

Considering the physicochemical characteristics of the studied hydrogel coatings alone, it appears that in particular, the C2A2 sample may offer the minimum CA value while maintaining reasonable vis-cosity and stability. It is also characterized by the most homogeneous structure with a negligible presence of micrometer-sized pores.

3.2. The influence of chitosan hydrogel cross-linking density on the charge transfer process

The influence of the chitosan hydrogel coating on the kinetics and reversibility of the electrode process was tested on three standard redox probes differing in the electric charge (Fig. 3). It turned out that for the $[Ru(NH_3)_6]^{2+}$ probe (Fig. 3a), the characteristic oxidation and reduction processes are significantly suppressed, compared to the unmodified GCE.

Likewise, the $FcDM^0$ probe kinetics, depicted in Fig. 3b, reveal similar irreversible characteristics. While the currents measured during the oxidation of electrically neutral $FcDM^0$ appear to be in a similar range compared to unmodified GCE, the reduction of $FcDM^+$ species is nearly completely blocked. Such results indicate the barrier properties of the positively charged surface of the chitosan hydrogel against cat-ions, due to the coulombic interactions that occur, limiting mass trans-port to the reaction surfaces. A likewise conclusion follows analysis for the negatively charged $[Fe(CN)_6]^{4-}$ probe (Fig. 3c), where the observed oxidation peak current value is triplicated after chitosan hydrogel deposition. Regarding $[Ru(NH_3)_6]^{2+}$, the observed response due to the oxidation/reduction reaction with the modified electrode surface is very small (Fig. 3a). Such an apparent limitation of the reaction kinetics is the result of the electrostatic interaction between the cationic polymer and the positively charged redox model. Mass transport (of the redox probe)
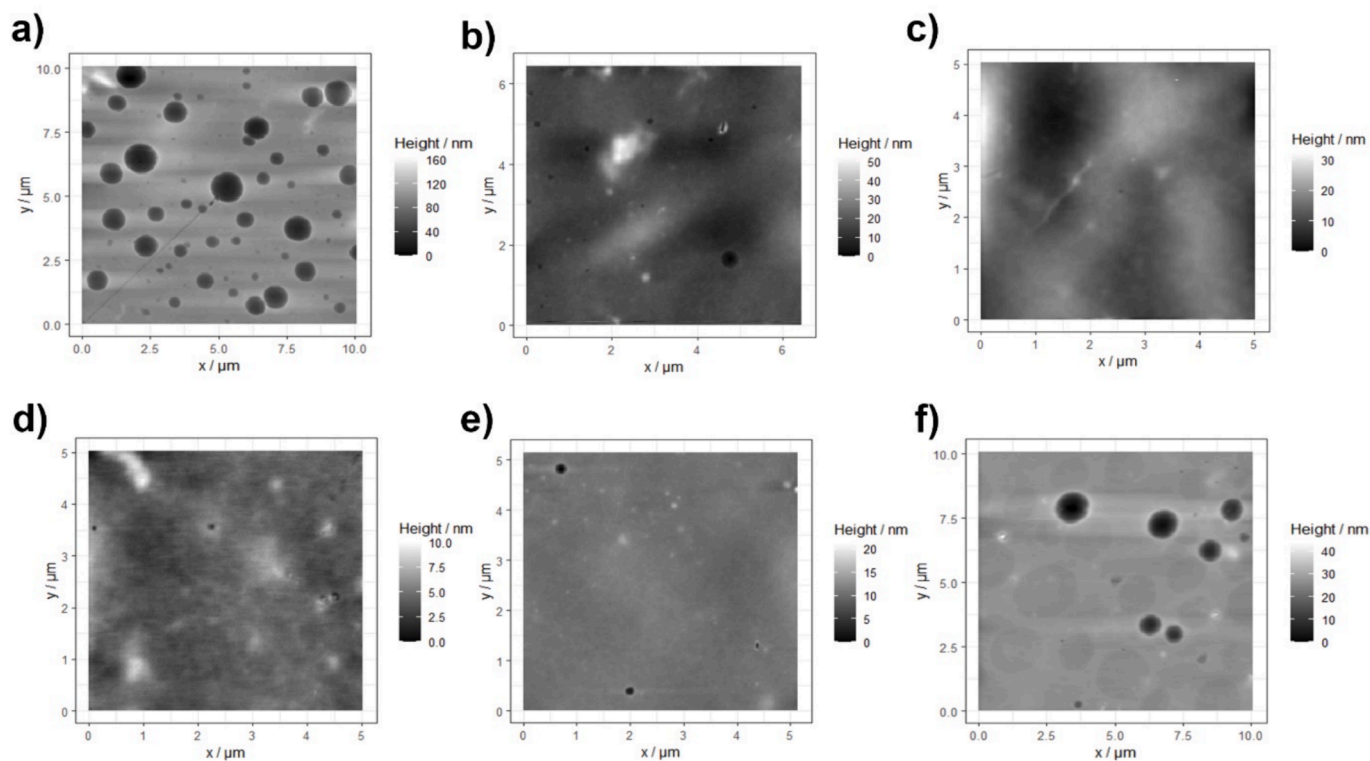

Fig. 2. AFM micrographs in semi-contact "tapping" mode for chitosan hydrogel-covered GCE samples with a-c) varying Cs concentration and d-f) varying Ga content: a) C1A2; b) C2A2; c) C4A2; d) C2A1; e) C2A3; f) C2A5.
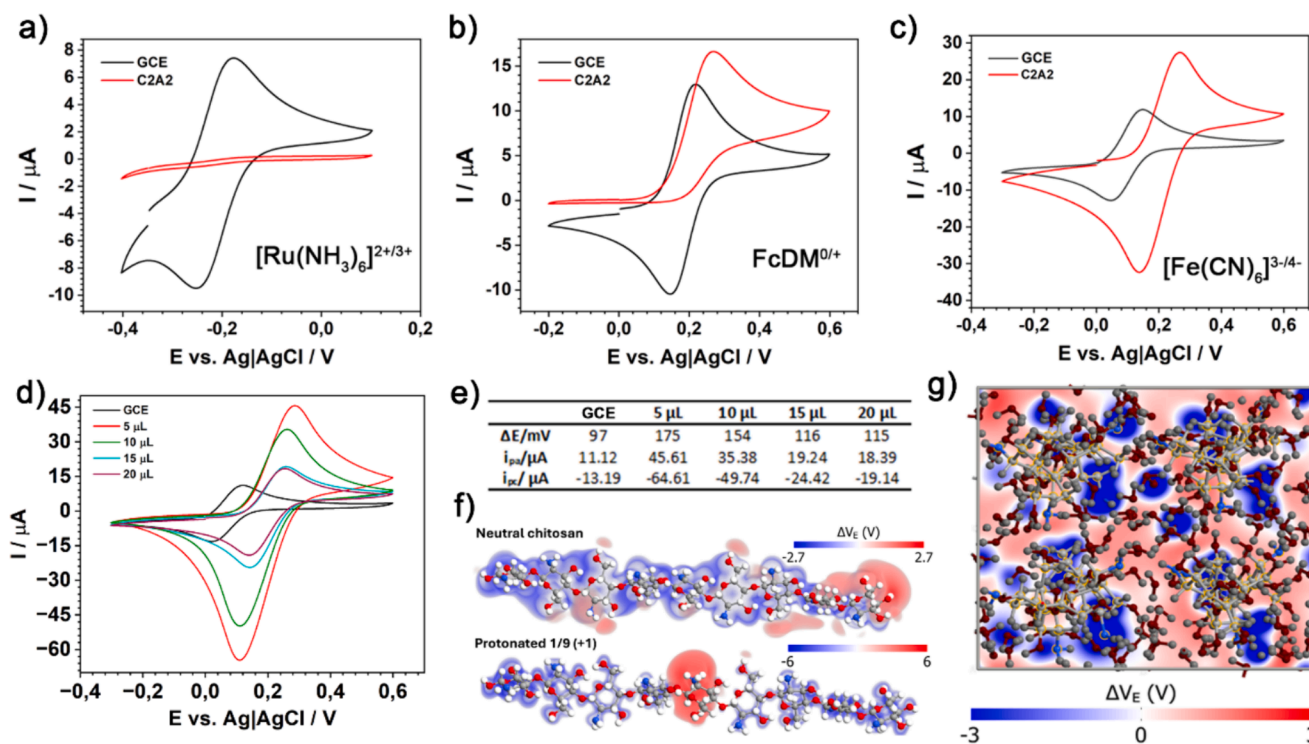
Fig. 3. A–c) Cyclic voltammetry (CV) for different redox probes: a) $[Ru(NH_3)_6]^{2+}$, b) $FcDM^0$, c) $[Fe(CN)_6]^{4-}$ ($\nu = 100$ mV/s, c = 1 mM) for C2A2 hydrogel coating surface engineered at GCE; d,e) the influence of hydrogel coating thickness (measured as the volume of grafted C2A2 hydrogel: 5 µL, 10 µL, 15 µL and 20 µL): d) CV scan ($\nu = 100$ mV/s, 1 mM $[Fe(CN)_6]^{4-}$ in PBS); e) kinetic parameters ΔE, $i_{p,a}$ and $|i_{p,c}|$; f,g) electrostatic potential maps from DFT calculations: f) chitosan molecule at neutral and protonated state, g) positive charge tunnels around NH_3^+ groups in cross-linked hydrogel coating.

to the surface is limited hindering the redox process. This result is connected with the electrostatic-driven alteration of process kinetics between positively charged chitosan chains with a redox probe (attraction for anions and repulsion for cations), affecting factors such as concentration of redox species, electrochemically-active surface area (EASA), diffusion coefficient D, and/or heterogeneous transfer rate k. One must note, however, that the three studied redox probes differ in the electron transfer mechanism, where $FcDM^0$ and $[Ru(NH_3)_6]^{2+}$ are characterized by outer sphere electron transfer by tunneling and $[Fe(CN)_6]^{4-}$ requires adsorption and direct interaction in the coordination sphere. Following the above-presented discussion, $[Fe(CN)_6]^{4-}$ appears to be the most suitable redox probe to be used with chitosan hydrogel, and thus it remained the focus within the next measurements. However, when compared to unmodified GCE, the values of $[Fe(CN)_6]^{3-/4-}$ reduction/oxidation potentials shift towards positive values indicating that both redox forms interact with the hydrogel structure. If the heterogeneous rate constant of the positively charged chitosan matrix with the $[Fe(CN)_6]^{4-}$ molecule is greater than the constant of the interaction with $[Fe(CN)_6]^{3-}$ then a shift in redox potentials toward increasingly positive values is observed. This may indicate an increase in the stability of one of the resulting redox forms with the chitosan matrix.

The thickness of the applied chitosan hydrogel coating (considered as a hydrogel volume, placed over a known GCE surface area) may significantly affect the electrochemical response. Fig. 3d depicts the CV curves studied for different volumes of the applied hydrogel, with kinetic parameters summarized in Fig. 3e. It appears that the biggest boost of the measured $[Fe(CN)_6]^{4-/3-}$ oxidation–reduction peak currents is achieved for the thinnest hydrogel coating, after applying 5 µL of chitosan. However, at the same time, the anodic-to-cathodic peak potential shift ΔE increases by nearly 70 mV, marking the inevitable increase in redox process irreversibility. Thus, a very interesting observation can be made, that the increase of the applied chitosan volume (up to 20 µL, studied in this experiment) eventually brings both redox currents and

ΔE closer to what is observed in the absence of hydrogel. The following may originate from the observation that thicker hydrogel coatings have a higher number of positively charged terminal mers, which might result in lower electrostatic effects. On the other hand, a thicker coating makes it more challenging to homogeneously cover the electrode surface, affecting the mass transport and diffusion field distribution [57]. The presence of micropores reported with AFM leads to local disturbances in the diffusion field, affecting electrochemical response.

According to electrostatic potential maps of the single, neutral chitosan chain, the positive charge is localized on the –OH groups and more concentrated on terminal structural units (Fig. 3f). This intriguing DFT calculation result was further discussed in the SI file, section S1. Conversely, in protonated chitosan the positive charge is strongly concentrated at each –NH_3^+ group. ESP maps yielding from the 4-chain periodic system reveal that the space between the chitosan chains (containing water molecules) is mostly positively charged, as seen in an ESP cross-section given in Fig. 3g. This result corroborates the idea of the formation of the positively charged tunnels inside the polymer, allowing faster transport of the negatively charged $[Fe(CN)_6]^{3-/4-}$ species. Macroscopically, this electrostatic phenomenon is presumably responsible for the preconcentration effects and thus the recorded CV shapes and current increase. In the frame of DFT results, a smaller thickness of the polymer might be more beneficial for electrochemical applications. In general, the coating on the surface decreases the diffusion coefficient, compared to the pristine solution – the polymer is an obstacle. However, short tunnels (on the order of the characteristic diffusion length) with positive charges might facilitate transport of ferrocyanide molecules via electrostatic interactions. Similar thing occurs in ion transport in lipid bilayers of biological cells e.g. voltage-gated K^+ or Na^+ channels [58]. Longer channels, on the other hand (longer than characteristic length of diffusion on the timescale of the process) might fail in this task. Even though the electrostatic effects might be present, they would effectively be suppressed by scattering associated with Brownian motion. Overall,

while preconcentration occurs in both cases, thinner coating might be more effective in transporting the preconcentrated molecules towards electrode.

The GCE surface engineering by hydrogel coatings with different Cs and Ga concentrations, giving consequences in hydrogel viscosity, charge distribution but also mass transport, have a significant influence on the redox process kinetics. This is schematically visualized in Fig. 4a.

The CV studies performed for different Ga and Cs content are depicted in Fig. 4b and c, respectively. The cross-linking effect on the CV kinetic parameters is visualized in Fig. 4d. Here, ΔE and $i_{p,a}$ denote anodic-to-cathodic peak current separation, indicating the redox process reversibility, and $[Fe(CN)_6]^{4-}$ to $[Fe(CN)_6]^{3-}$ oxidation peak current, respectively. Based on the obtained results, one can conclude that an increase in current response is visible for all proposed hydrogels with the addition of chitosan (C1-C3), yet too high a Cs concentration (C4) may impair the kinetics of the electrode process. This effect is assisted by large surface pores distribution originating from sub-optimal viscosity.

On the other hand, it appears that the cross-linker (Ga) has a less vital influence on the charge transfer kinetics, which seems to be primarily connected to electrode hydrophilicity increase at low Ga content. An observable increase in CV peak currents remains up to a certain cross-linker density (A4) when electron transfer is suffocated. It is assumed that as the concentration of Ga increases, the cross-linking density increases, lowering the possibilities of the structural arrangement of the hydrogel, due to the progressive rigidity of the entire chitosan structure.

This indicates more difficult conditions in electron transfer and diffusion of analytes into the deeper layers of the hydrogel, expressed by a decrease in the CV peak currents. More detailed electrochemical studies are presented in the SI file, section S2.

An overall conclusion should be made, that too high cross-linking density causes difficulties in reaching the actual electrode surface and introducing heterogeneous structural features for interaction with the analyte, consequently affecting the electron transfer. Considering both electrochemical and physicochemical criteria, we have selected C2A2 hydrogel with its slight derivatives, C2A3 and C3A2, for further electrode kinetics studies.

3.3. Preconcentration of the analyte by the chitosan hydrogel coating

The EIS spectra in the Nyquist projection for the selected samples are shown in Fig. 5a and 5b. Each spectrum is composed of a single time constant – implying a single charge transfer process – and a diffusion tail in a low-frequency range characteristic of diffusion-controlled redox process. The semicircle diameter for each studied surface-engineered sample is significantly smaller compared to the pristine GCE sample. A simple Randles electric equivalent circuit (EEC), $R_e(C_{dl}(R_{ct}W))$, was used for detailed data analysis. Here, R_S stands for the series resistance (dominated by the electrolyte resistance), R_{CT} is the charge transfer resistance, C_{DL} is the electric double-layer capacitance and Warburg element W models the diffusion process. Results of the non-linear least
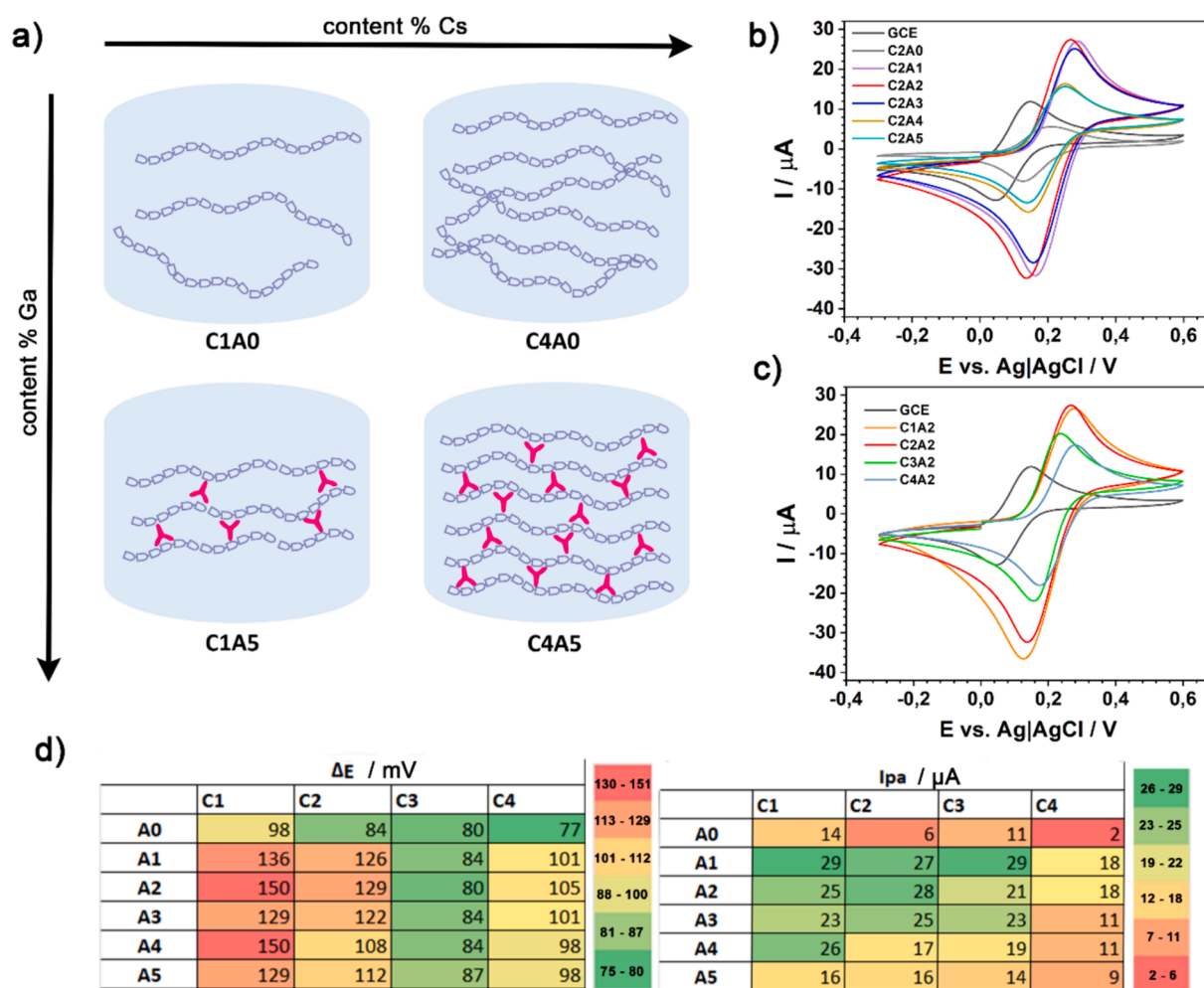

Fig. 4. a) schematic illustration of Cs and Ga influence on cross-linking density; b,c) exemplary CV curves recorded for hydrogel coating ($\nu = 100$ mV/s, 1 mM [Fe(CN)$_6$]$^{4-}$ in PBS) at GCE surface, hydrogels with varying content of b) Ga crosslinker; c) Cs; d) CV kinetic parameters ΔE and $i_{p,a}$ for differently engineered hydrogel coatings. Colors indicate effective parameters from red (worse) to green (preferable).
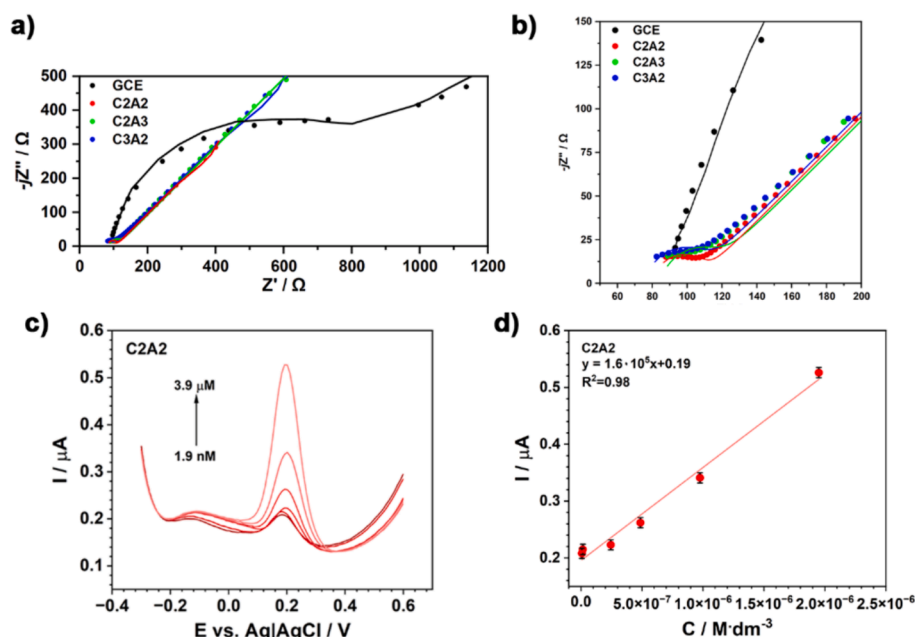
Fig. 5. a,b) EIS measurements for GCE and selected hydrogels (C2A2, C2A3, C3A2); c) DPV studies for $[Fe(CN)_6]^{4-}$ at various concentrations; d) calibration curve and $[Fe(CN)_6]^{4-}$ LOD calculation for C2A2 sample.

squares fitting of the data are summarized in Table 3.

The R_{CT} values for each electrode with different chitosan hydrogel coatings decreased about 20× compared to unmodified GCE. For a one-step, one-electron process at low overpotentials and assuming the charge transfer coefficient α = 0.5, the use of Eq. (3) allows us to conclude that the R_{CT} drop may be connected either to the increase in heterogeneous rate constant k, or increase in the concentration of redox species inside the coating C*, or an increase in A (EASA) [59,60].

$$R_{CT} = \frac{2RT}{n^2 F^2 AkC} \quad (3)$$

Considering chitosan hydrogel is ionically conductive, the charge transfer phenomenon likely occurs on the GCE-chitosan interface (electronic conduction is very unlikely due to the high electronic band gap resulting from aliphatic structure with all single bonds). Thus, its presence should not notably affect the EASA. This hypothesis is supported by comparable C_{DL} values regardless of the hydrogel coating and negligible hydrogel influence on electrode hydrophilicity. Only a small increase in C_{DL} value is observable due to the increase in electric permittivity ε, according to Eq. (4).

Table 3
The EIS parameters (R_S, R_{CT}, C_{DL}, Y_W and χ^2), charge transfer rate, analyte concentration within the diffusion layer C* and LOD, calculated for unmodified GCE and selected chitosan-modified samples: C2A2, C2A3, and C3A2.

	GCE	C2A2	C2A3	C3A2
R_S	115.2	83.2	84.2	78.0
C_{DL}/µF	1.26	1.79	2.28	1.66
R_{CT}/Ω	667.0	27.9	31.0	33.5
Y_W/mSs$^{0.5}$	0.27	1.40	0.98	0.93
$\chi^2 \times 10^{-3}$/–	7.08	6.60	6.76	6.24
k/cm/s	1.14×10^{-2}	1.14×10^{-2}	1.14×10^{-2}	1.14×10^{-2}
C*/mM	1 (assume)	19.5	17.6	16.2
D/cm^2/s	2.64×10^{-7}	1.87×10^{-8}	1.12×10^{-8}	1.09×10^{-8}
LOD [Fe(CN)$_6$]$^{4-}$/nM	101	0.20	0.25	0.29

$$C_{DL} = \frac{\varepsilon_0 \varepsilon A}{d} \quad (4)$$

where ε_0 is vacuum permittivity, d is electric double-layer thickness and A is EASA.

The charge transfer rate is also not expected to change significantly after the hydrogel modification because the gel does not directly participate in the charge transfer. Indeed, changes in the distribution of the charge density accumulated in the Stern layer induced by the chitosan dipoles might indirectly impact the oxidation and reduction rates. The result of this impact is the slight asymmetry of the CV peaks observed in Fig. 4b and c.

Nevertheless, the main factor determining the changes in R_{CT} is assumed to be the preconcentration of the ferrocyanide molecules inside the polymer, which effectively changes the concentration gradient in the diffusion layer, and thus the measured current. Preconcentration of negatively charged ferrocyanide molecules in the gel is possible due to the presence of positively charged tunnels shown in ESP (Fig. 3f,g) maps and in agreement with ζ-potential measurements in Fig. 1b,e.

Assuming that in the case of the pristine GCE, there is no pre-concentration, and the EASA is equal to the geometric area, one can calculate the charge transfer rate based on R_{CT}, which is equal to 1.14×10^{-2} cm/s. It is to be noted that this value might be overestimated due to the non-negligible development of the GCE surface area. In the following step effective concentrations of ferrocyanides in the chitosan were calculated based on R_{CT} of C2A2, C2A3, and C3A2 samples. Results lie in the interval 16–20 mM, which strongly suggests preconcentration (see Table 3).

Warburg admittance Y_W increases after modifications, suggesting that the hydrogel facilitates diffusion of the ferrocyanide. However, an increase in the diffusion coefficient inside the hydrogel is unlikely due to the steric hindrance, which is expected to reduce the mean-free path characteristic length. The diffusion coefficient of the ferrocyanide in the case of pristine GCE was estimated to be 2.64×10^{-7} cm^2/s based on Eqs. (5) and (6) [59]:

$$Z_W = \frac{A_W}{\sqrt{j\omega}} \quad (5)$$

$$A_W = \frac{1}{Y_W} = \frac{RT}{2n^2F^2A\sqrt{D}C^*} \tag{6}$$

Although the D value is underestimated – presumably due to the limitations of the Warburg model – the exact value is not relevant to the discussion. The important aspect is that after taking the preconcentration effect into account in Eq. (5), the effective diffusion coefficient in the modified samples decreases, even though the Warburg admittances increase. Analogous results were obtained for the glucose preconcentration in Nafion, where despite a lower diffusion coefficient, the performance in glucose sensing was higher [61].

Such an outcome is expected due to the viscosity and permeability effects elucidated in the previous sections. Diffusion layer thickness typically ranges from several to several hundred nanometers, depending on the ionic strength of the electrolyte, while the applied hydrogel coating is micrometer-sized. Thus, it should be considered that effective concentrations refer to the interior of the chitosan hydrogel coating rather than 1 mM $[Fe(CN)_6]^{4-}$ in the aqueous PBS electrolyte. As a consequence, the most likely explanation of the enhancement of amperometric response is the hydrogel boosting the ferrocyanides ions concentration in the hydrogel volume C^*. The preconcentration is a result of ions migration from PBS due to the opposite electrostatic charge between the chitosan hydrogel and the redox species. Notably EIS-measured lower series resistance R_S value for each chitosan hydrogel coating modification, compared to unmodified GCE, corroborates the increase in ionic conductivity.

Considering the above discussion, the hydrogel's primary action appears to be by increasing the transport properties driven by electrostatic interactions between the redox probe and chitosan hydrogel moieties.

In terms of electrode sensitivity, surface-engineered and unmodified GCEs were compared toward $[Fe(CN)_6]^{3-/4-}$ detection limits in KCl solution, using the DPV, see Fig. 5e and f. LOD was estimated using the relationship given by Eq. (7).

$$LOD = 3.3(Sy/S) \tag{7}$$

with Sy denoting the relative standard deviation measured in the low concentration range and S is the slope of the calibration curve. The data obtained show a significant improvement in the analytical characteristics of the modified electrode compared to the unmodified one. A set of characteristic current peaks with linearly increasing values is observed for both electrodes. As a result of the modification of the electrode, a slight shift toward a positive potential is observed compared to the GCE. For the hydrogel-covered electrode, the lowest LOD value obtained is 0.20 nM for C2A2 modification, whereas for the GCE the LOD was three orders of magnitude higher, and equal to 0.1 μM. This study also reveals that slight changes in hydrogel composition do not drastically affect the electrode sensitivity, as the LOD for C2A3 and C3A3 was estimated to be 0.25 and 0.29 nM, respectively. The LOD for other hydrogel coatings at GCE are summarized in the SI file, section S3. Our studies indicate the high potential of the obtained modifications in electroanalytical applications. The observed improvement in the LOD of the modified electrodes is a result of the accelerating diffusion transport at the electrode/electrolyte interface.

4. Conclusion

Chitosan hydrogels were applied on GCE electrodes for electroanalytical utility. The ratio of chitosan (Cs) to glutaraldehyde (Ga) determines the crosslinking density, hydrogel rheology, and consequently mass-transport characteristics – thus its optimization is important. High chitosan concentrations yield increased viscosity and slower diffusion. Low crosslinker results in poor permeation due to decreased hydrophilicity, while too high Ga content leads to micropore formation within the hydrogel as shown by AFM, introducing electric heterogeneity and

affecting diffusion. While the measured ζ-potential for each hydrogel exceeded 40 mV noting their high stability, it might be decreased by too high a Cs concentration.

DFT analysis suggested the existence of positively charged tunnels between chitosan chains, boosted by the presence of the $-NH_3^+$ group and $-OH$ protons and terminal structural units, revealed by XPS analysis. Such electrostatic milieu in the hydrogel interior suppresses the currents of $[Ru(NH_3)_6]^{2+}$ redox couple and elevates the response of $[Fe(CN)_6]^{4-}$, while not affecting electrically-neutral $FcDM^0$.

Chitosan-modified electrodes exhibited enhanced electroanalytical performance justified by the electrostatic migration of the negative ions into the hydrogel, increasing the effective concentration. As a result, effective $[Fe(CN)_6]^{4-}$ LOD with surface-engineered GCE is also improved from 100 down to even 0.2 nM. Detailed CV and EIS studies show a negligible role of both the heterogeneous rate transfer and the electrochemically active surface area when considering the effect of GCE surface engineering.

CRediT authorship contribution statement

Declaration of competing interest

The authors declare the following financial interests/personal relationships which may be considered as potential competing interests: Jacek Ryl reports was provided by National Science Centre Poland. If there are other authors, they declare that they have no known competing financial interests or personal relationships that could have appeared to influence the work reported in this paper.

Data availability

Data will be made available on request.

Acknowledgments

Appendix A. Supplementary data

Supplementary data to this article can be found online at https://doi.org/10.1016/j.bioelechem.2024.108804.

References

[1] S. Singh, J. Wang, S. Cinti, Review—An overview on recent progress in screen-printed electroanalytical (bio)sensors, ECS Sens. Plus 1 (2022) 023401, https://doi.org/10.1149/2754-2726/ac70e2.

[2] R.D. Crapnell, C.E. Banks, Electroanalytical overview: utilising micro- and nano-dimensional sized materials in electrochemical-based biosensing platforms, Microchim. Acta 188 (2021) 268, https://doi.org/10.1007/s00604-021-04913-y.

[3] R.D. Crapnell, C.E. Banks, Electroanalysis overview: addressing the green credentials in the use of electroanalytical sensors, Green Carbon 1 (2023) 85–93, https://doi.org/10.1016/j.greenca.2023.09.003.

[4] V. Uskoković, A historical review of glassy carbon: synthesis, structure, properties and applications, Carbon Trends 5 (2021) 100116, https://doi.org/10.1016/j.cartre.2021.100116.

[5] I. Švancara, K. Vytřas, K. Kalcher, A. Walcarius, J. Wang, Carbon paste electrodes in facts, numbers, and notes: a review on the occasion of the 50-years jubilee of carbon paste in electrochemistry and electroanalysis, Electroanalysis 21 (2009) 7–28, https://doi.org/10.1002/elan.200804340.

[6] K. Muzyka, G. Xu, Laser-induced graphene in facts, numbers, and notes in view of electroanalytical applications: a review, Electroanalysis 34 (2022) 574–589, https://doi.org/10.1002/elan.202100425.

[7] S. Baluchová, A. Daňhel, H. Dejmková, V. Ostatná, M. Fojta, K. Schwarzová-Pecková, Recent progress in the applications of boron doped diamond electrodes in electroanalysis of organic compounds and biomolecules – a review, Anal. Chim. Acta 1077 (2019) 30–66, https://doi.org/10.1016/j.aca.2019.05.041.

[8] X. Xu, X. Niu, X. Li, Z. Li, D. Du, Y. Lin, Nanomaterial-based sensors and biosensors for enhanced inorganic arsenic detection: a functional perspective, Sens. Actuators B Chem. 315 (2020) 128100, https://doi.org/10.1016/j.snb.2020.128100.

[9] A. Pahlavan, V.K. Gupta, A.L. Sanati, F. Karimi, M. Yoosefian, M. Ghadami, ZnO/CNTs nanocomposite/ionic liquid carbon paste electrode for determination of noradrenaline in human samples, Electrochim. Acta 123 (2014) 456–462, https://doi.org/10.1016/j.electacta.2014.01.006.

[10] B.J. Sanghavi, A.K. Srivastava, Simultaneous voltammetric determination of acetaminophen, aspirin and caffeine using an in situ surfactant-modified multiwalled carbon nanotube paste electrode, Electrochim. Acta 55 (2010) 8638–8648, https://doi.org/10.1016/j.electacta.2010.07.093.

[11] Y. Sheng, W. Qian, J. Huang, B. Wu, J. Yang, T. Xue, Y. Ge, Y. Wen, Electrochemical detection combined with machine learning for intelligent sensing of maleic hydrazide by using carboxylated PEDOT modified with copper nanoparticles, Microchim. Acta 186 (2019) 543, https://doi.org/10.1007/s00604-019-3652-x.

[12] C. Mao, D. Yuan, L. Wang, E. Bakker, Separating boundary potential changes at thin solid contact ion transfer voltammetric membrane electrodes, J. Electroanal. Chem. 880 (2021) 114800, https://doi.org/10.1016/j.jelechem.2020.114800.

[13] N. Vladislavić, I.Š. Rončević, M. Buzuk, M. Buljac, I. Drventić, Electrochemical/chemical synthesis of hydroxyapatite on glassy carbon electrode for electroanalytical determination of cysteine, J. Solid State Electrochem. 25 (2021) 841–857, https://doi.org/10.1007/s10008-020-04856-z.

[14] T. Liljeström, K.S. Kontturi, V. Durairaj, N. Wester, T. Tammelin, T. Laurila, J. Koskinen, Protein adsorption and its effects on electroanalytical performance of nanocellulose/carbon nanotube composite electrodes, Biomacromolecules 24 (2023) 3806–3818, https://doi.org/10.1021/acs.biomac.3c00449.

[15] K. Marcisz, K. Kaniewska, M. Karbarz, Smart functionalized thin gel layers for electrochemical sensors, biosensors and devices, Curr. Opin. Electrochem. 23 (2020) 57–64, https://doi.org/10.1016/j.coelec.2020.03.011.

[16] K. Marcisz, K. Kaniewska, Z. Stojek, M. Karbarz, Electroresponsiveness of a positively charged thin hydrogel layer on an electrode surface, Electrochem. Commun. 125 (2021) 106981, https://doi.org/10.1016/j.elecom.2021.106981.

[17] I. Shitanda, R. Asano, Y. Hoshi, M. Itagaki, K. Takada, An Electrochemical actuator fabricated by transfer-printing of a carbon electrode onto a cupric-ion-containing poly(acrylic acid) gel surface, Electrochemistry 88 (2020) 236–239, https://doi.org/10.5796/electrochemistry.19-00063.

[18] X. Xia, Q. Liang, X. Sun, D. Yu, X. Huang, S.M. Mugo, W. Chen, D. Wang, Q. Zhang, Intrinsically electron conductive, antibacterial, and anti-swelling hydrogels as implantable sensors for bioelectronics, Adv. Funct. Mater. 32 (2022) 2208024, https://doi.org/10.1002/adfm.202208024.

[19] G.S. Kassahun, S. Griveau, S. Juillard, J. Champavert, A. Ringuedé, B. Bresson, Y. Tran, F. Bedioui, C. Slim, Hydrogel matrix-grafted impedimetric aptasensors for the detection of diclofenac, Langmuir 36 (2020) 827–836, https://doi.org/10.1021/acs.langmuir.9b02031.

[20] R. Baretta, A. Raucci, S. Cinti, M. Frasconi, Porous hydrogel scaffolds integrating Prussian Blue nanoparticles: a versatile strategy for electrochemical (bio)sensing, Sens. Actuators B Chem. 376 (2023) 132985, https://doi.org/10.1016/j.snb.2022.132985.

[21] C.-L. Ke, F.-S. Deng, C.-Y. Chuang, C.-H. Lin, Antimicrobial actions and applications of chitosan, Polymers 13 (2021) 904, https://doi.org/10.3390/polym13060904.

[22] M. Iriti, E.M. Varoni, Chitosan-induced antiviral activity and innate immunity in plants, Environ. Sci. Pollut. Res. 22 (2015) 2935–2944, https://doi.org/10.1007/s11356-014-3571-7.

[23] F. Avelelas, A. Horta, L.F.V. Pinto, S. Cotrim Marques, P. Marques Nunes, R. Pedrosa, S.M. Leandro, Antifungal and antioxidant properties of chitosan polymers obtained from nontraditional Polybius Henslowii sources, Mar. Drugs 17 (2019) 239, https://doi.org/10.3390/md17040239.

[24] I.A. Sogias, A.C. Williams, V.V. Khutoryanskiy, Why is chitosan mucoadhesive? Biomacromolecules 9 (2008) 1837–1842, https://doi.org/10.1021/bm800276d.

[25] T. Kean, M. Thanou, Biodegradation, biodistribution and toxicity of chitosan, Adv. Drug Deliv. Rev. 62 (2010) 3–11, https://doi.org/10.1016/j.addr.2009.09.004.

[26] C. Peniche, W. Argüelles-Monal, H. Peniche, N. Acosta, Chitosan: an attractive biocompatible polymer for microencapsulation, Macromol. Biosci. 3 (2003) 511–520, https://doi.org/10.1002/mabi.200300019.

[27] S. Bautista-Banos (Ed.), Chitosan in the Preservation of Agricultural Commodities, Elsevier; AP, Amsterdam, 2016.

[28] J. Fu, F. Yang, Z. Guo, The chitosan hydrogels: from structure to function, New J. Chem. 42 (2018) 17162–17180, https://doi.org/10.1039/C8NJ03482F.

[29] D. Nataraj, S. Sakkara, N. Meghwal, N. Reddy, Crosslinked chitosan films with controllable properties for commercial applications, Int. J. Biol. Macromol. 120 (2018) 1256–1264, https://doi.org/10.1016/j.ijbiomac.2018.08.187.

[30] M.A. Mohammed, J.T.M. Syeda, K.M. Wasan, E.K. Wasan, An overview of chitosan nanoparticles and its application in non-parenteral drug delivery, Pharmaceutics 9 (2017) 53, https://doi.org/10.3390/pharmaceutics9040053.

[31] S. Yalçınkaya, C. Demetgül, M. Timur, N. Çolak, Electrochemical synthesis and characterization of polypyrrole/chitosan composite on platinum electrode: Its electrochemical and thermal behaviors, Carbohydr. Polym. 79 (2010) 908–913, https://doi.org/10.1016/j.carbpol.2009.10.022.

[32] A.N. Annu, Raja, Recent development in chitosan-based electrochemical sensors and its sensing application, Int. J. Biol. Macromol. 164 (2020) 4231–4244, https://doi.org/10.1016/j.ijbiomac.2020.09.012.

[33] L.D. Nguyen, T.C.D. Doan, T.M. Huynh, V.N.P. Nguyen, H.H. Dinh, D.M.T. Dang, C.M. Dang, An electrochemical sensor based on polyvinyl alcohol/chitosan-thermally reduced graphene composite modified glassy carbon electrode for sensitive voltammetric detection of lead, Sens. Actuators B 345 (2021) 130443, https://doi.org/10.1016/j.snb.2021.130443.

[34] X. Li, N. Falcone, M.N. Hossain, H.-B. Kraatz, X. Chen, H. Huang, Development of a novel label-free impedimetric electrochemical sensor based on hydrogel/chitosan for the detection of ochratoxin A, Talanta 226 (2021) 122183, https://doi.org/10.1016/j.talanta.2021.122183.

[35] N.H.N. Do, Q.T. Truong, P.K. Le, A.C. Ha, Recent developments in chitosan hydrogels carrying natural bioactive compounds, Carbohydr. Polym. 294 (2022) 119726, https://doi.org/10.1016/j.carbpol.2022.119726.

[36] T. Furuike, D. Komoto, H. Hashimoto, H. Tamura, Preparation of chitosan hydrogel and its solubility in organic acids, Int. J. Biol. Macromol. 104 (2017) 1620–1625, https://doi.org/10.1016/j.ijbiomac.2017.02.099.

[37] S.M. Alshehri, T. Almuqati, N. Almuqati, E. Al-Farraj, N. Alhokbany, T. Ahamad, Chitosan based polymer matrix with silver nanoparticles decorated multiwalled carbon nanotubes for catalytic reduction of 4-nitrophenol, Carbohydr. Polym. 151 (2016) 135–143, https://doi.org/10.1016/j.carbpol.2016.05.018.

[38] W. Lian, S. Liu, J. Yu, X. Xing, J. Li, M. Cui, J. Huang, Electrochemical sensor based on gold nanoparticles fabricated molecularly imprinted polymer film at chitosan–platinum nanoparticles/graphene–gold nanoparticles double nanocomposites modified electrode for detection of erythromycin, Biosens. Bioelectron. 38 (2012) 163–169, https://doi.org/10.1016/j.bios.2012.05.017.

[39] A. Nawaz, B. Islam, M.Z. Ijaz, U. Saleem, M. Sadiq Khattak, S.N. Ahmad, N. Maqsood, L. Ali, An alternative and indirect statistical modeling method for viscosity estimation and its experimental validation for low styrene content polyester resin, Pol. J. Chem. Technol. 20 (2018) 60–65, https://doi.org/10.2478/pjct-2018-0055.

[40] L. Martínez, R. Andrade, E.G. Birgin, J.M. Martínez, P ACKMOL : A package for building initial configurations for molecular dynamics simulations, J. Comput. Chem. 30 (2009) 2157–2164, https://doi.org/10.1002/jcc.21224.

[41] G. Lawrie, I. Keen, B. Drew, A. Chandler-Temple, L. Rintoul, P. Fredericks, L. Grøndahl, Interactions between alginate and chitosan biopolymers characterized using FTIR and XPS, Biomacromolecules 8 (2007) 2533–2541, https://doi.org/10.1021/bm070014y.

[42] J. Zawadzki, H. Kaczmarek, Thermal treatment of chitosan in various conditions, Carbohydr. Polym. 80 (2010) 394–400, https://doi.org/10.1016/j.carbpol.2009.11.037.

[43] M.C. Biesinger, Accessing the robustness of adventitious carbon for charge referencing (correction) purposes in XPS analysis: Insights from a multi-user facility data review, Appl. Surf. Sci. 597 (2022) 153681, https://doi.org/10.1016/j.apsusc.2022.153681.

[44] A. Koterwa, I. Kaczmarzyk, S. Mania, M. Cieslik, R. Tylingo, T. Ossowski, R. Bogdanowicz, P. Niedziałkowski, J. Ryl, The role of electrolysis and enzymatic hydrolysis treatment in the enhancement of the electrochemical properties of 3D-printed carbon black/poly(lactic acid) structures, Appl. Surf. Sci. 574 (2022) 151587, https://doi.org/10.1016/j.apsusc.2021.151587.

[45] P.-C. Li, G. Liao, S.R. Kumar, C.-M. Shih, C.-C. Yang, D.-M. Wang, S.J. Lue, Fabrication and characterization of chitosan nanoparticle-incorporated quaternized poly(vinyl alcohol) composite membranes as solid electrolytes for direct methanol alkaline fuel cells, Electrochim. Acta 187 (2016) 616–628, https://doi.org/10.1016/j.electacta.2015.11.117.

[46] M. Ficek, K.J. Sankaran, J. Ryl, R. Bogdanowicz, I.-N. Lin, K. Haenen, K. Darowicki, Ellipsometric investigation of nitrogen doped diamond thin films grown in microwave CH4/H2/N2 plasma enhanced chemical vapor deposition, Appl. Phys. Lett. 108 (2016) 241906, https://doi.org/10.1063/1.4953779.

[47] E. Szczepańska, B. Grobelna, J. Ryl, A. Kulpa, T. Ossowski, P. Niedziałkowski, Efficient method for the concentration determination of Fmoc groups incorporated in the core-shell materials by Fmoc-glycine, Molecules 25 (2020) 3983, https://doi.org/10.3390/molecules25173983.

[48] P. Xiong, L. Zhang, Y. Chen, S. Peng, G. Yu, A chemistry and microstructure perspective on ion-conducting membranes for redox flow batteries, Angew. Chem., Int. Ed. 60 (2021) 24770–24798, https://doi.org/10.1002/anie.202105619.

[49] L. Gao, H. Gan, Z. Meng, R. Gu, Z. Wu, L. Zhang, X. Zhu, W. Sun, J. Li, Y. Zheng, G. Dou, Effects of genipin cross-linking of chitosan hydrogels on cellular adhesion and viability, Colloids Surf. B Biointerfaces 117 (2014) 398–405, https://doi.org/10.1016/j.colsurfb.2014.03.002.

[50] Y. Li, C. Chen, Synthesis of ambient copolymerization CQAS hydrogel composite membrane with enhanced antifouling, Adv. Mater. Interfaces 9 (2022) 2201226, https://doi.org/10.1002/admi.202201226.

[51] A. Al-Amoudi, P. Williams, A.S. Al-Hobaib, R.W. Lovitt, Cleaning results of new and fouled nanofiltration membrane characterized by contact angle, updated DSPM, flux and salts rejection, Appl. Surf. Sci. 254 (2008) 3983–3992, https://doi.org/10.1016/j.apsusc.2007.12.052.

[52] R. Foudazi, R. Zowada, I. Manas-Zloczower, D.L. Feke, Porous hydrogels: present challenges and future opportunities, Langmuir 39 (2023) 2092–2111, https://doi.org/10.1021/acs.langmuir.2c02253.

[53] M. Zhang, T. Zhao, J. Dou, Z. Xu, W. Zhang, X. Chen, X. Wang, B. Zhou, Bottom-up construction of conjugated microporous polyporphyrin-coated graphene hydrogel composites with hierarchical pores for high-performance capacitors, ChemElectroChem 6 (2019) 5946–5950, https://doi.org/10.1002/celc.201901586.

[54] D. Jain, A. Karajic, M. Murawska, B. Goudeau, S. Bichon, S. Gounel, N. Mano, A. Kuhn, P. Barthélémy, Low-molecular-weight hydrogels as new supramolecular materials for bioelectrochemical interfaces, ACS Appl. Mater. Interfaces 9 (2017) 1093–1098, https://doi.org/10.1021/acsami.6b12890.

[55] T.J. Davies, C.E. Banks, R.G. Compton, Voltammetry at spatially heterogeneous electrodes, J. Solid State Electrochem. 9 (2005) 797–808, https://doi.org/10.1007/s10008-005-0699-x.

[56] J. Ryl, L. Burczyk, A. Zielinski, M. Ficek, A. Franczak, R. Bogdanowicz, K. Darowicki, Heterogeneous oxidation of highly boron-doped diamond electrodes and its influence on the surface distribution of electrochemical activity, Electrochimica Acta 297 (2019) 1018–1027, https://doi.org/10.1016/j.electacta.2018.12.050.

[57] A.J. Bard, L.R. Faulkner, H.S. White, Electrochemical Methods: Fundamentals and Applications, Third edition, Wiley, Hoboken, NJ, 2022.

[58] C.-L.-H. Huang, Keynes & Aidley's Nerve and Muscle, 5th ed., Cambridge University Press, 2020 doi: 10.1017/9781108860789.

[59] A. Lasia, Electrochemical Impedance Spectroscopy and its Applications, Springer, New York, New York, NY, 2014 doi: 10.1007/978-1-4614-8933-7.

[60] J. Wysocka, S. Krakowiak, J. Ryl, Evaluation of citric acid corrosion inhibition efficiency and passivation kinetics for aluminium alloys in alkaline media by means of dynamic impedance monitoring, Electrochim. Acta 258 (2017) 1463–1475, https://doi.org/10.1016/j.electacta.2017.12.017.

[61] A. Olejnik, J. Karczewski, A. Dołęga, K. Siuzdak, K. Grochowska, Insightful analysis of phenomena arising at the metal│polymer interphase of Au-Ti based non-enzymatic glucose sensitive electrodes covered by Nafion, Coatings 10 (2020) 810, https://doi.org/10.3390/coatings10090810.